Eleventh International Conference on Computational Fluid Dynamics (ICCFD11), Maui, Hawaii, USA, July 11-15, 2022 **ICCFD11-2022-1002**

A high-order low-dissipation Euler–Lagrange method for compressible gas-particle flows

Meet Patel*, Jesse Capecelatro**
Corresponding author: meetm@umich.edu

* Research Assistant, University of Michigan, Ann Arbor, Michigan, 48109.
** Associate Professor, University of Michigan, Ann Arbor, Michigan, 48109.

Abstract: We present a low-dissipation strategy for simulating gas-particle compressible flows from dilute to dense concentrations. The volume-filtered compressible Navier–Stokes equations are discretized using high-order energy stable finite difference operators with localized shock capturing. Particle are tracked individually in a Lagrangian manner and undergo collisions and exchange momentum and heat with the gas. A ghost-point immersed boundary method is used to handle complex geometries on Cartesian grids. The framework is applied to three-dimensional simulations of underexpanded jets impinging on a granular bed under varying nozzle pressure ratios.

*The work is funded via NASA award no. 80NSSC20K0295.

Keywords: Compressible flow, Lagrangian particle tracking, Jet impingement

1 Introduction

Particle-laden compressible flows can be found in many environmental and engineering applications, such as volcanic eruptions [3], coal dust explosions [20], pulsed detonation engines [43], solid propellant combustion [22], and plume-surface interactions during powered descent of a spacecraft [30, 1, 5]. Compared to its low-speed counterpart, high-speed (compressible) particle-laden flows involve considerably different flow physics, such as the emergence of compression and expansion waves, and sometimes bow shocks upstream of particles when the flow is supersonic. Such flow structures produce sharp gradients in gas-phase properties that modify aerodynamic forces acting on the particles. Thus, simulating such flows requires special attention, as most efforts to date have focused on the incompressible regime.

Parmar et al. [39, 40] extended the equations of motion for an isolated particle in a viscous incompressible fluid to viscous compressible flows. They show that gas-phase compressibility affects the particle dynamics through a combination of quasi-steady and unsteady forces. Despite the high density ratios associated with gas-solid flows, unsteady forces (Basset history and added mass) can exhibit leading order effects during shock-particle interactions [37, 24]. Particle-resolved simulations have recently shown that a shock wave passing through a cloud of particles at moderate volume fractions can generate small-scale velocity fluctuations termed pseudo-turbulent kinetic energy (PTKE) [31, 35, 36, 32, 44]. In such situations, particles create a nozzling effect that chokes the flow due to abrupt changes in volume fraction [49]. Shallcross et al. [44] developed a model for PTKE that arises during shock-particle interactions, which was shown to be critical for capturing this choking behavior in simulations based on averaged equations. The purpose of this work is to introduce a numerical framework for employing such models.

Numerically simulating compressible gas-particle flows can be handled in several ways. Particle resolved direct numerical simulations (PR-DNS) apply sub-particle grid resolution such that the a direct solution to the conservation equations can be obtained with appropriate boundary conditions enforced at the surface of each particle (e.g., [29, 35, 19, 48]). Despite its accuracy, the high computational demand limits the number of particles to $\mathcal{O}(10^3)$. Eulerian–Lagrangian (EL) methods typically apply grid spacing larger than the particle diameter, such that interphase coupling is handled through source terms while particle collisions are directly captured [25, 6]. EL methods rely on subgrid-scale models often developed from PR-DNS. Due to the reduced computational cost, EL simulations are capable of handling $\mathcal{O}(10^8)$ particles (e.g., see [4]). An alternative approach is to model the particle phase as another fluid phase, referred as the two-fluid or Eulerian-Eulerian (EE) model [1, 12]. While EE does not have a limitation on the number of particles, it relies heavily on constitutive models for the solid phase.

In this work, we present an EL framework tailored for compressible turbulent flows laden with solid particles. The gas-phase equations are discretized using high-order energy stable finite difference operators on structured grids. Localized artificial diffusivity is employed for shock capturing. Special care is taken when coupling these methods with immersed boundaries when handling complex geometries. A soft-sphere collision model is employed for particle collisions. The framework is applied to simulations of an underexpanded jet impinging on a bed of solid particles. The effect of nozzle pressure ratio on crater morphology is studied.

2 Numerics

2.1 Volume-Filtered Gas-Phase Equations

Volume filtering the viscous compressible Navier–Stokes equations (excluding the volume occupied by particles) yields a set of gas-phase equations at a scale larger than individual particles [44]. The volume-filtered equations can be expressed compactly as

$$\frac{\partial \boldsymbol{Q}}{\partial t} + \frac{\partial}{\partial x_i}\left[\alpha\left(\boldsymbol{F}_i^I - \boldsymbol{F}_i^V\right)\right] = \boldsymbol{S}, \tag{1}$$

where $\boldsymbol{Q} = [\alpha\rho, \alpha\rho u_i, \alpha\rho E]^T$ is the vector of conserved variables, $\boldsymbol{F}^V$ and $\boldsymbol{F}^I$ are the viscous and inviscid fluxes, respectively, and $\boldsymbol{S}$ contains source terms that account for two-way coupling and acceleration due to gravity, g_i, given by

$$\boldsymbol{F}_i^I = \begin{bmatrix} \rho u_i \\ \rho u_1 u_i + p\delta_{i1} \\ \rho u_2 u_i + p\delta_{i2} \\ \rho u_3 u_i + p\delta_{i3} \\ u_i(\rho E + p) \end{bmatrix}, \quad \boldsymbol{F}_i^V = \begin{bmatrix} 0 \\ \tau_{1i} \\ \tau_{2i} \\ \tau_{3i} \\ u_j\tau_{ij} - q_i \end{bmatrix}, \quad \boldsymbol{S} = \begin{bmatrix} 0 \\ (p\delta_{i1} - \tau_{i1})\frac{\partial\alpha}{\partial x_i} + \mathcal{F}_1 + g_1 \\ (p\delta_{i2} - \tau_{i2})\frac{\partial\alpha}{\partial x_i} + \mathcal{F}_2 + g_2 \\ (p\delta_{i3} - \tau_{i3})\frac{\partial\alpha}{\partial x_i} + \mathcal{F}_3 + g_3 \\ (\tau_{ij} - p\delta_{ij})\frac{\partial}{\partial x_i}(\alpha_p u_{p,j}) + q_i\frac{\partial\alpha}{\partial x_i} + u_{p,i}\mathcal{F}_i + \mathcal{Q} \end{bmatrix}.$$

The conserved variables include the the gas-phase volume fraction α, density ρ, velocity u_i (in direction i), and total energy E. The particle volume fraction is $\alpha_p = 1 - \alpha$. Pressure is related to energy according to $p = (\gamma - 1)(\rho E - \rho u_i u_i/2)$, where $\gamma = 1.4$ is the ratio of specific heats.

The viscous stress tensor and heat flux are given by

$$\tau_{ij} = \mu \left(\frac{\partial u_i}{\partial x_j} + \frac{\partial u_j}{\partial x_i} \right) + \left(\beta - \frac{2}{3}\mu \right) \frac{\partial u_k}{\partial x_k} \delta_{ij} \quad \text{and} \quad q_i = -\kappa \frac{\partial T}{\partial x_i}, \tag{2}$$

where κ is the thermal conductivity, T is the temperature obtained from the ideal gas law, μ is the dynamic (shear) viscosity that has a power law dependence on temperature, and β is the bulk viscosity. Finally, $\mathcal{F}_i$ and $\mathcal{Q}_i$ appearing in $\boldsymbol{S}$ are the interphase momentum and heat exchange terms, respectively, that will be defined in Sec. 2.6.

2.2 High-order Energy Stable Discretization

The gas-phase equations are discretized using high-order finite difference operators that admit low artificial dissipation. Kinetic energy preservation is achieved using a skew-symmetric-type splitting of the inviscid flux [42], extended to account for the volume fraction. This provides nonlinear stability at low Mach number. The convective fluxes appearing in (1) are expressed in split form as

$$\frac{\partial \alpha\rho u_i \varphi}{\partial x_i} = \frac{1}{2}\frac{\partial \alpha\rho u_i \varphi}{\partial x_i} + \frac{1}{2}\varphi \frac{\partial \alpha\rho u_i}{\partial x_i} + \alpha\rho u_i \frac{\partial \varphi}{\partial x_i}, \tag{3}$$

where φ is a generic transported scalar, which is unity for the continuity equation, u_j for the momentum equation, and $E + p/\rho$ for the total energy equation. Spatial derivatives are approximated using narrow-stencil finite difference operators D_i that satisfy the summation-by-parts (SBP) property [45]

$$PD + (PD)^{\mathsf{T}} = \operatorname{diag}\left[-1,\ 0,\ \ldots,\ 0,\ 1\right]^{\mathsf{T}}, \tag{4}$$

where P is a symmetric positive-definite matrix and $D \in \mathbb{R}^{N \times N}$. This leads to $2s$-order centered-difference stencils at interior points and s-order accurate biased stencils near boundaries, with $s+1$ global accuracy. The sixth-order interior formulation ($s = 3$) is considered in the present work. To evaluate second and mixed derivatives, first derivative operators are applied consecutively, necessitating the use of artificial dissipation to damp the highest wavenumber components supported by the grid. High-order accurate SBP dissipation operators are used that provide artificial viscosity based on a $2s$-order derivative [27].

The SBP scheme is combined with the simultaneous approximation treatment (SAT) at the domain boundaries to facilitate an energy estimate [7, 34]. This is achieved by enforcing the desired boundary conditions in a weak sense by adding a penalty term to the right-hand-side of the governing equations. Non-reflecting characteristic boundary conditions and no-penetration free-slip walls are considered in the present work. Following the notation in Svärd et al. [47], Svärd and Nordström [46], the SAT treatment for far-field boundary conditions applied to the left boundary in one direction (with analogous treatment applied to the right boundary and the other two directions), is given by

$$\frac{\partial \boldsymbol{Q}}{\partial t} = R(\boldsymbol{Q}) + \sigma^I P^{-1} E_1 A^+ \left(\hat{\boldsymbol{Q}} - \hat{\boldsymbol{Q}}_b \right) - \sigma^V P^{-1} E_1 \left(\boldsymbol{F}^V - \boldsymbol{F}_b^V \right), \tag{5}$$

where $R(\boldsymbol{Q})$ is the right-hand side of the compressible flow equations, σ^I and σ^V are inviscid and viscous penalty parameters, respectively. $E_1 = [1,\ 0,\ \ldots,\ 0]^{\mathsf{T}}$ ensures the penalty is only applied at the domain boundary, and A^+ is the Roe matrix that selects the incoming characteristics. Setting $\sigma^I \leq -1/2$ and $\sigma^V = -1$ ensures numerical stability (with opposite signs for the right boundary) [47]. The boundary data are supplied through a stationary target solution in the vector $\hat{\boldsymbol{Q}}_b(\boldsymbol{x})$ and $\boldsymbol{F}_b^V(\boldsymbol{Q}_b)$. The specific form used to enforce far-field non-reflecting characteristic boundary conditions and no-penetration free-slip walls are given in Vishnampet

Ganapathi Subramanian [50]. When $\alpha > 0$, we find using $\hat{\boldsymbol{Q}} = \boldsymbol{Q}/\alpha$ is needed for the inviscid terms and when evaluating A^{+}. In addition, an absorbing sponge region [14] is applied at the domain boundary to prevent unphysical acoustic reflections by adding a damping term of the form $\Psi(\boldsymbol{x})\left[\boldsymbol{Q}(\boldsymbol{x},t) - \boldsymbol{Q}_b(\boldsymbol{x})\right]$ to the right-hand side of the conservation equations.

The equations are advanced in time using a standard fourth-order Runge–Kutta scheme, resulting in the usual Courant–Friedrichs–Lewy (CFL) restrictions on the simulation time step Δt. The CFL is taken as the maximum between the acoustic CFL, $\mathrm{CFL}_a = \max\left(|\boldsymbol{u}| + c\right)\Delta t/\Delta$ and the viscous CFL, $\mathrm{CFL}_v = \max\left(2\mu, \beta, \kappa\right)\Delta t/\Delta^2$, where Δ is the local grid spacing and $c = \sqrt{\gamma p/\rho}$ is the local sound speed.

2.3 Shock Capturing

Localized artificial diffusivity is used as a means of shock capturing following the 'LAD-D2-0' formulation in Kawai et al. [21]. Here, the bulk viscosity and thermal conductivity appearing in Eq. (2) are augmented according to $\beta = \beta_f + \beta^*$ and $\kappa = \kappa_f + \kappa^*$, where the subscript f and asterisks denote fluid and artificial transport coefficients, respectively. The artificial dissipation terms take the form

$$\beta^* = C_\beta \overline{\rho f_{sw} |\nabla^4 \theta|} \Delta^6, \quad \kappa^* = C_\kappa \overline{\frac{\rho c}{T} |\nabla^4 e|} \Delta^5, \tag{6}$$

where $\theta = \nabla \cdot \boldsymbol{u}$, $e = (\gamma - 1)^{-1} p/\rho$, $C_\beta = 1$, and $C_\kappa = 0.01$. The overbar denotes a truncated 9-point Gaussian filter [9]. Fourth derivatives are approximated via a sixth-order compact (Padè) finite-difference operator [23]. To limit the artificial bulk viscosity to regions of high compression (shocks), we employ a similar sensor originally proposed by Ducros et al. [11] and later improved by Hendrickson et al. [18], given by $f_{sw} = \min\left(\frac{4}{3} H(-\theta) \times \frac{\theta^2}{\theta^2 + \Omega^2 + \epsilon}, 1\right)$, where H is the Heaviside function, $\epsilon - 10^{-32}$ is a small positive constant to prevent division by zero, and $\Omega = \max\left(|\nabla \times \boldsymbol{u}|, 0.05c/\Delta\right)$ is a frequency scale that ensures the sensor tends to zero where vorticity is negligible.

2.4 Immersed Boundary Method

A ghost-point immersed boundary method (IBM) is employed to handle complex geometries (like the nozzle in Sec. 3) on Cartesian grids, as shown in Fig. 1. The origin of this approach can be traced to Mohd-Yusof [33], which was extended to compressible flows by Chaudhuri et al. [8]. A signed distance levelset function $\mathcal{I}$ is used to distinguish interior (solid) and exterior (fluid) grid points (i.e., $\mathcal{I} < 0$ within the solid, $\mathcal{I} > 0$ outside). Values of the conserved variables at ghost points residing within the solid are assigned after each Runge–Kutta sub-iteration. A normal vector outward from the surface, $\boldsymbol{n} = \nabla \mathcal{I}$, is defined to locate the image of the corresponding ghost point in the fluid domain. Because image points do not align with grid points, fluid quantities are interpolated to image points via an inverse distance weighting scheme proposed by Chaudhuri et al. [8]. The number of layers of ghost points grows with increasing order of accuracy of the scheme. For the sixth-order interior finite difference stencil used herein, this requires 3 layers of grid points for first derivatives. However, for second derivatives, the number of layers are further extended.

Neumann boundary conditions are imposed for temperature and pressure by assigning the value of the ghost point equal to its image point. Dirichlet boundary conditions are enforced for velocity (i.e., no-slip). This is traditionally handled by assigning the velocity at the ghost point a value equal and opposite to the velocity at the image point. This was found to be numerically unstable for the high-order low dissipative scheme used in the present work. Instead, all ghost-points are assigned values of zero velocity.

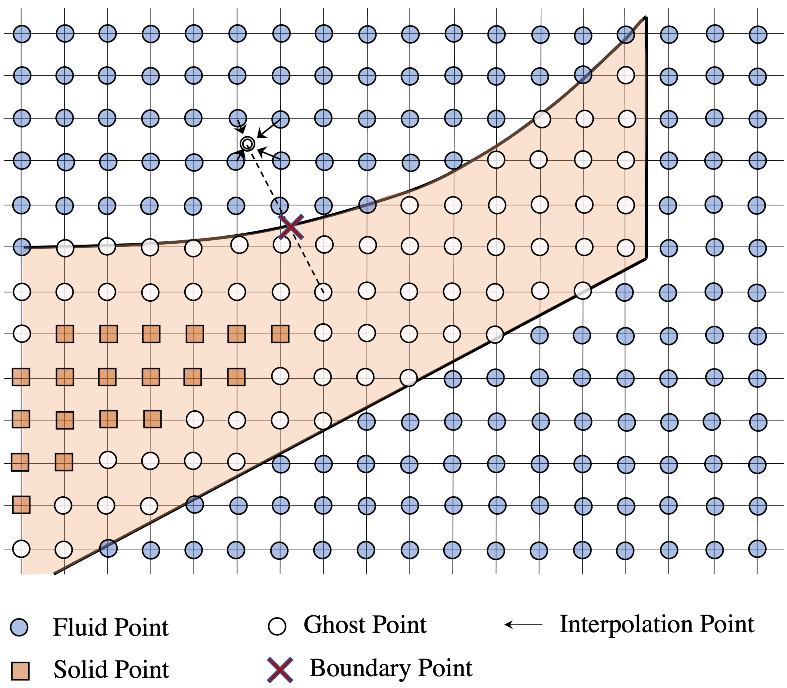

Figure 1: Schematic of the ghost point immersed boundary method with two layers of ghost points.

Applying the ghost point IBM to geometries with sharp corners presents further challenges [8, 2]. Boukharfane et al. [2] proposed solving an additional set of equations using the stencils from all sides of the corner (3 sides in three dimensions) to prescribe values at ghost-points. Alternatively, Chaudhuri et al. [8] proposed storing multiple arrays of ghost-points to use them according the flux direction, however this is an expensive approach to evaluate derivatives and is potentially memory intensive. We propose a simple and efficient alternative by applying the same truncated Gaussian filter used during shock capturing in Eq. (6) to the conserved variables at the interior points. The filter smears out discontinuities near corners while values away from discontinuities remain relatively unchanged (see Fig. 2). It was also found that filtering interior points avoids spurious oscillations and promotes stability.

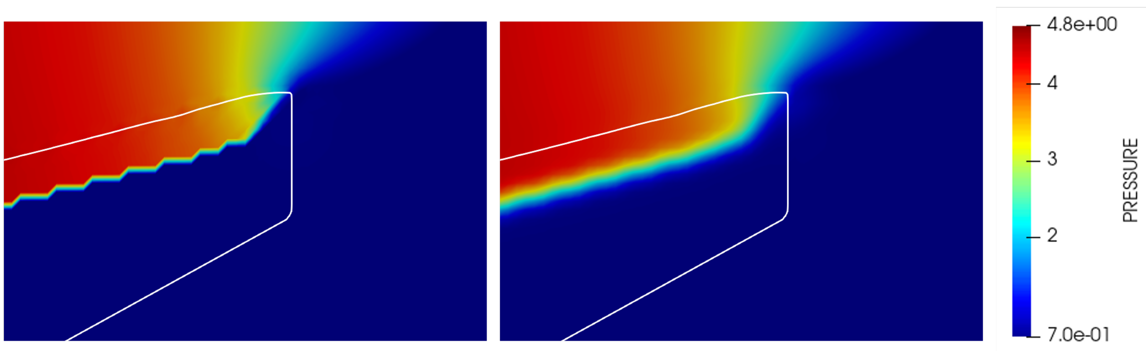

Figure 2: Left: pressure field in the vicinity of the nozzle lip. Right: pressure field after application of the truncated Gaussian filter applied to interior (solid) points. Contour of zero levelset (white line).

It is important to note that in the presence of strong discontinuities, the artificial diffusivity terms used for shock capturing (6) may induce a severe time-step restriction. To avoid introducing unphysical discontinuities near the immersed interface, β^* and κ^* are defined at every grid point within the domain (interior and exterior), but values inside the solid ($\mathcal{I} < 0$) are not used when computing CFL_v.

2.5 Lagrangian Particle Tracking

The equation of motion for an individual particle in a compressible flow has been recently derived [39, 40]. In this work, we neglect the unsteady force contributions, as closed-form expressions for $\alpha < 1$ do not yet exist, and the particle equations reduce to

$$\frac{\mathrm{d}\boldsymbol{x}_p^{(i)}}{\mathrm{d}t} = \boldsymbol{v}_p^{(i)} \tag{7}$$

$$m_p \frac{\mathrm{d}\boldsymbol{v}_p^{(i)}}{\mathrm{d}t} = V_p \nabla \cdot (\boldsymbol{\tau} - p\mathbf{I}) + \boldsymbol{F}_{\text{drag}}^{(i)} + \boldsymbol{F}_{\text{lift}}^{(i)} + \boldsymbol{F}_{\text{col}}^{(i)} + m_p \boldsymbol{g}, \tag{8}$$

where $\boldsymbol{x}_p^{(i)}$ and $\boldsymbol{v}_p^{(i)}$ are the position and velocity of particle i, respectively, m_p is the mass of the particle and V_p is its volume. $\boldsymbol{F}_{\text{drag}}^{(i)}$, $\boldsymbol{F}_{\text{lift}}^{(i)}$, and $\boldsymbol{F}_{\text{col}}^{(i)}$ are force contributions due to drag, lift, and collisions, respectively. The quasi-steady drag force is given by

$$\frac{\boldsymbol{F}_{\text{drag}}^{(i)}}{m_p} = \frac{F_d}{\tau_p} \alpha \left(\boldsymbol{u} - \boldsymbol{v}_p^{(i)} \right), \tag{9}$$

where $\tau_p = \rho_p d_p^2/(18\mu)$ is the Stokes response time and $F_d = F_d(\alpha_p, \mathrm{Re}_p)$ is the non-dimensional drag correlation of Gidaspow [15] and $\mathrm{Re}_p = \alpha\rho|\boldsymbol{u} - \boldsymbol{v}_p^{(i)}|d_p/\mu$ is the particle Reynolds number. It should be noted that while many drag correlations with Mach number corrections (e.g., [17, 26, 38]), no drag laws currently exist for finite Mach number *and* volume fraction (i.e., $F_d(\alpha_p, \mathrm{Re}_p, \mathrm{Ma}_p)$). This is currently being developed by the authors. The Saffman lift force is modeled according to [28]

$$\boldsymbol{F}_{\text{lift}}^{(i)} = \frac{9.69\sqrt{\rho\mu}}{\pi\rho_p d_p} \frac{(\boldsymbol{u} - \boldsymbol{v}_p^{(i)}) \times \boldsymbol{\omega}}{\sqrt{|\omega|}}, \tag{10}$$

where $\boldsymbol{\omega} = \nabla \times \boldsymbol{u}$ is the gas-phase vorticity. The force due to particle collisions, $\boldsymbol{F}_{\text{col}}^{(i)}$, is accounted for using the soft-sphere collision model proposed by Cundall and Strack [10]. Collisions are treated as inelastic with coefficient of restitution $e = 0.85$ and resolved over 30 timesteps [6]. To avoid excessive overlap between particles, the simulation timestep is restricted such that particles do not travel more than one-tenth of their diameter per time step. Particle rotation is taken into account according to

$$I_p \frac{\mathrm{d}\omega_{\mathrm{p}}^{(\mathrm{i})}}{\mathrm{d}t} = \boldsymbol{M}_{\text{col}}^{(i)}, \tag{11}$$

where $I_p = m_p d_p/10$ is moment of inertia of particle and $\boldsymbol{M}_{\text{col}}^{(i)}$ is torque that arises from tangential collisions [6] and using coefficient of friction $\mu_f = 0.4$ to imitate sand particles and soil properties on Mars.

The evolution of particle temperature is given by

$$m_p C_{p,p} \frac{\mathrm{d}T_p^{(i)}}{\mathrm{d}t} = q_{\text{inter}}^{(i)}, \tag{12}$$

where $C_{p,p}$ is heat capacity of the particle, $T_p^{(i)}$ is its temperature, and $q_{\text{inter}}^{(i)}$ is the interphase heat exchange given by

$$q_{\text{inter}}^{(i)} = \frac{6V_p \kappa \text{Nu}}{d_p^2}\left(T - T_p^{(i)}\right), \tag{13}$$

where the Nusselt number Nu is modeled using the correlation of Gunn [16]. It should be noted that here both phases are advanced in time simultaneously using the standard fourth-order Runge–Kutta scheme.

2.6 Two-Way Coupling

Fluid quantities (velocity, temperature, volume fraction, etc.) are transferred to each particle via trilinear interpolation. Particle information (drag, heat exchange, volume fraction, etc.) is sent back to the Eulerian grid using the two-step filtering approach proposed by Capecelatro and Desjardins [6]. The volume fraction is computed according to

$$\alpha(\boldsymbol{x}, t) = 1 - \sum_{1}^{N_p} \mathcal{G}\left(|\boldsymbol{x} - \boldsymbol{x}_p^{(i)}|\right) V_p, \tag{14}$$

where $\mathcal{G}$ is a Gaussian filter kernel with a characteristic length $\delta_f = 4d_p$ and N_p is the total number of particles. The momentum exchange term is given by

$$\boldsymbol{\mathcal{F}} = -\sum_{i=1}^{N_p} \mathcal{G}\left(|\boldsymbol{x} - \boldsymbol{x}_p^{(i)}|\right)\left(\boldsymbol{F}_{\text{drag}}^{(i)} + \boldsymbol{F}_{\text{lift}}^{(i)}\right). \tag{15}$$

Similarly, work due to momentum exchange appearing in the energy equation (2.1) is given by

$$\boldsymbol{u}_p \cdot \boldsymbol{\mathcal{F}} = -\sum_{i=1}^{N_p} \mathcal{G}\left(|\boldsymbol{x} - \boldsymbol{x}_p^{(i)}|\right)\left(\boldsymbol{F}_{\text{drag}}^{(i)} + \boldsymbol{F}_{\text{lift}}^{(i)}\right) \cdot \boldsymbol{v}_p^{(i)}. \tag{16}$$

Similarly, the interphase heat exchange term appearing in the energy equation (1) is given by

$$\mathcal{Q} = -\sum_{i=1}^{N_p} \mathcal{G}\left(|\boldsymbol{x} - \boldsymbol{x}_p^{(i)}|\right) q_{\text{inter}}^{(i)}. \tag{17}$$

2.7 Stability Criterion

In the absence of two-way coupling, the simulation timestep is restricted by the acoustic and viscous time scales according to the typical CFL conditions discussed in the previous sections. However, in the presence of particles with two-way coupling, the interphase source terms can impose an additional time-step restriction. In low-pressure conditions these terms become numerically stiff [41]. For simplicity, neglecting non-conservative terms and gravity in $\boldsymbol{S}$, the interphase exchange terms appearing in (2.1) can be expressed in vector form as $\boldsymbol{S} = [0, \mathcal{F}_1, \mathcal{F}_2, \mathcal{F}_3, \boldsymbol{u}_p \cdot \boldsymbol{\mathcal{F}}]^T$. Neglecting lift forces for simplicity $\boldsymbol{\mathcal{F}}$ can be written as

$$\boldsymbol{\mathcal{F}} = \begin{bmatrix} (u - u_p) 18\alpha\mu(1-\alpha)F_d/d_p^2 \\ (v - v_p) 18\alpha\mu(1-\alpha)F_d/d_p^2 \\ (w - w_p) 18\alpha\mu(1-\alpha)F_d/d_p^2 \end{bmatrix}. \tag{18}$$

Differentiating with respect to the state variables, and assuming F_d is independent of state variables, the Jacobian matrix is

$$\partial \boldsymbol{S}/\partial \boldsymbol{Q} = \begin{bmatrix} 0 & 0 & 0 & 0 & 0 \\ 0 & \dfrac{18\mu(1-\alpha)F_d}{\rho d_p^2} & 0 & 0 & 0 \\ 0 & 0 & \dfrac{18\mu(1-\alpha)F_d}{\rho d_p^2} & 0 & 0 \\ 0 & 0 & 0 & \dfrac{18\mu(1-\alpha)F_d}{\rho d_p^2} & 0 \\ 0 & \dfrac{18\mu(1-\alpha)u_pF_d}{\rho d_p^2} & \dfrac{18\mu(1-\alpha)v_pF}{\rho d_p^2} & \dfrac{18\mu(1-\alpha)w_pF}{\rho d_p^2} & 0 \end{bmatrix}. \tag{19}$$

The corresponding Eigenvalues are $\lambda_d = [0,\ 0,\ \tau_d^{-1},\ \tau_d^{-1},\ \tau_d^{-1}]$, where $\tau_d^{-1} = 18\mu(1-\alpha)F_d/(\rho d_p^2)$. Implicit treatment of the interphase exchange terms is in general challenging due to its Lagrangian nature. Therefore, we retain an explicit treatment and ensure the time step is sufficiently small. For the fourth-order Runge–Kutta scheme used here, this requires $\Delta t < 2.75\ \tau_d$.

3 Underexpanded Jet Impinging on a Granular Bed

3.1 Simulation Setup

The framework is applied to a three-dimensional simulation of an under-expanded jet impinging on a bed of settled particles (see Fig. 3). The nozzle geometry is modeled as a converging section based on a hyperbolic tangent function with an initial straight section [52]. The nozzle has diameter D and is placed $H = 3.75D$ above the bed of particles. The domain of size $6D \times 40D \times 40D$ is discretized on a Cartesian grid of size $247 \times 883 \times 883$ with uniform grid spacing in the streamwise direction and stretching is applied in the spanwise directions ($\Delta z = \Delta y_{\min} = \Delta x_{\min} = D/40$ and $\Delta y_{\max} = \Delta x_{\max} = D/8$). An auxiliary simulation was performed to settle the particles and achieve the random close-packing limit to a desired bed height of $1.3D$ and a bed diameter of $12D$. The particles are monodisperse with diameter $d_p = 0.0157D$. Additionally, the peripheral particles of the bed are enforced to stay in place to imitate an infinitely long boundary. The ambient pressure p_∞ and density ρ_∞ are chosen to be 101325 $\mathrm{N/m^2}$ and 1.2 $\mathrm{kg/m^3}$, respectively, and density ratio $\rho_p/\rho_\infty = 2.08 \times 10^3$.

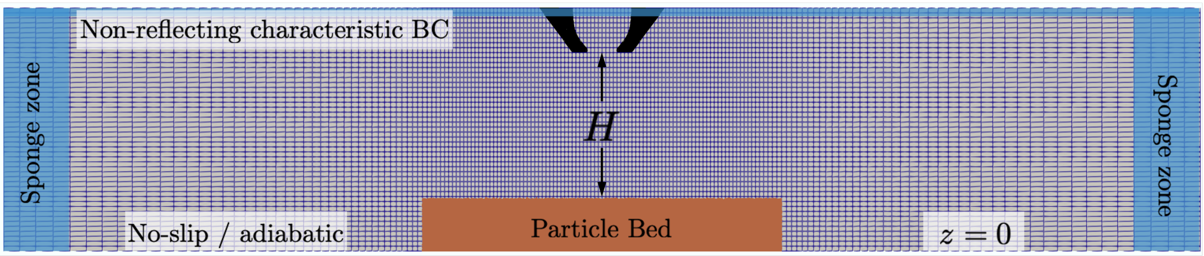

Figure 3: Simulation setup.

A two-dimensional snapshot of the grid and boundary conditions is shown in the Fig. 3. The top and spanwise boundaries are non-reflecting to allow acoustic disturbances to leave while the bottom boundary is treated as no-slip and adiabatic. Within the nozzle, inlet conditions (i.e., pressure, temperature, and velocity) are prescribed based on isentropic relations. This allows for sonic conditions (i.e., $\mathrm{Ma} \equiv U/c = 1$ with U velocity of the jet) at the nozzle exit. The pressure at the inlet represents the tank pressure and is chosen to achieve a desired nozzle pressure ratio (NPR). The NPR correlates with the degree of underexpansion and variations in the structure of the jet [13]. In this work, the NPR is set to 4.08 and 6.12 such that at higher NPR, a finite size Mach disk is observed making the jet look qualitatively different. The jet Reynolds number, $\mathrm{Re}_D \equiv \rho U D/\mu = 1.38 \times 10^6$ for NPR $= 4.08$ and $\mathrm{Re}_D = 2.06 \times 10^6$ for NPR $= 6.12$.

3.2 Results

Owing to the different characteristics of the jet at two different pressure ratios, we observe entirely different crater shapes at time, $tD/U \approx 68$. Figure 4 shows a constant surface of $\alpha_p = 0.4$ to visualize the particle bed and resulting crater along with the two-dimensional slice of the local gas-phase Mach number. The crater morphology is distinctly different between the two pressure rations. A "U"-shaped crater is observed at lower NPR while at higher NPR, a "W"-shaped crater is observed due to presence of a Mach disk. The particle jet in the center of the crater resembles a Worthington jet observed in gas-liquid flows [51].

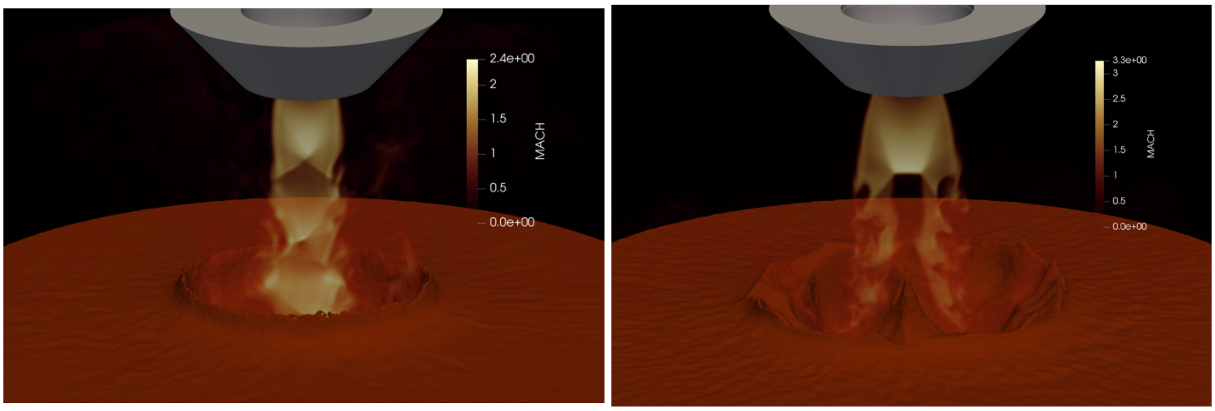

Figure 4: Instantaneous snapshots of the underexpanded jet impinging on a bed of particle at $tD/U \approx 68$ with NPR$= 4.08$ (left) and NPR$= 6.12$ (right). Gas-phase Mach number shown in red/yellow. Iso-surface of $\alpha_p = 0.4$ (brown) defining the bed and crater morphology.

To better understand the input/output relationship between NPR and crater shape, Fig. 5 shows a comparison the pressure field at $tD/U \approx 27$. It is noticeable that pressure field just above the top layer of particles are distinct. At low NPR, high pressure is focused in the stagnation zone, causing particles to evacuate radially outward, giving rise to the "U"-shaped crater. At higher NPR, the formation of a Mach disk causes a bifurcation in pressure, resulting in low pressure at the axes and the build up of particles.

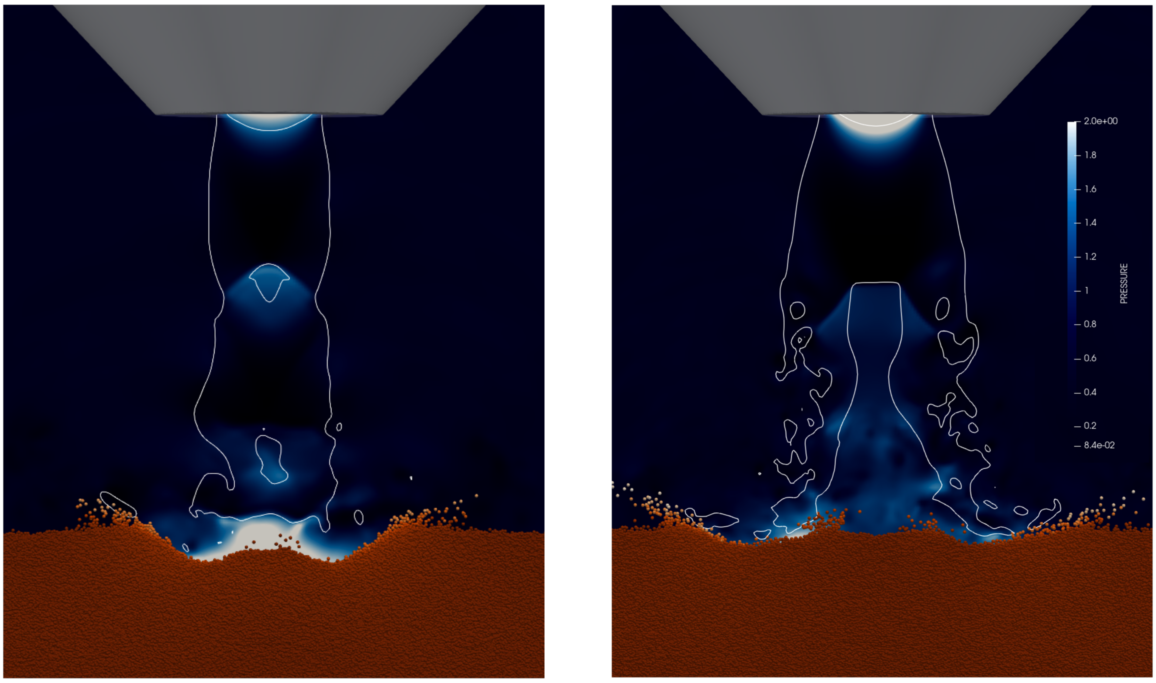

Figure 5: Instantaneous snapshots of the gas-phase pressure field (blue) at $tD/U \approx 27$ with NPR= 4.08 (left) and NPR= 6.12 (right). Ma $= 1$ contour (white line). Particles are colored by their velocity magnitude with lighter shade representing higher velocities and vice-versa.

4 Conclusions

We present a high-order low-dissipation numerical framework tailored for particle-laden compressible flows. Detailed are provided for the coupling between the high-order discretization, shock capturing, immersed boundaries, and Lagrangian particle tracking. The ghost point immersed boundary method is modified to account for complex geometries in the presence of strong discontinuities. We also present the additional CFL stability criterion that needs to be satisfied when two-way coupling is enabled. The added stability criterion does not add any further restrictions beyond the usual acoustic time step except under low densities ($\sim 1\%$ of Earth's atmosphere). The framework is applied to simulations of underexpanded jets impinging on the settled particles at two different pressure ratios. It is found that the pressure distribution on the surface of the particle bed is significantly different between the two nozzle pressure ratios, resulting in distinctively different cratering.

The framework presented herein provides a basis to implement improved subgrid-scale models. Many challenges still exist. For example, it remains unclear how to properly reconstruct fluid quantities at the particle location in the presence of strong discontinuities like shocks when evaluating drag and lift. New models are also needed for the forces acting on particles valid for a wide range of Reynolds numbers, Mach numbers, and volume fractions.

References

[1] K. Balakrishnan and J. Bellan. High-fidelity modeling and numerical simulation of cratering induced by the interaction of a supersonic jet with a granular bed of solid particles. *International Journal of Multiphase Flow*, 99:1–29, 2018.

[2] R. Boukharfane, F. Henrique E. Ribeiro, Z. Bouali, and A. Mura. A combined ghost-point-forcing/direct-forcing immersed boundary method (IBM) for compressible flow simulations. *Computers & Fluids*, 162:91–112, 2018.

[3] S. M. Bower and A. W. Woods. On the dispersal of clasts from volcanic craters during small explosive eruptions. *Journal of Volcanology and Geothermal Research*, 73(1):19 – 32, 1996. ISSN 0377-0273.

[4] D.A. Buchta, G. S. Shallcross, and J. Capecelatro. Sound and turbulence modulation by particles in high-speed shear flows. *Journal of Fluid Mechanics*, 875:254–285, 2019.

[5] J. Capecelatro. Modeling high-speed gas–particle flows relevant to spacecraft landings. *International Journal of Multiphase Flow*, page 104008, 2022.

[6] J. Capecelatro and O. Desjardins. An Euler–Lagrange strategy for simulating particle-laden flows. *Journal of Computational Physics*, 238:1–31, 2013.

[7] M.H. Carpenter, D. Gottlieb, and S Abarbenel. Time-stable boundary conditions for finite difference schemes involving hyperbolic systems: methodology and application for high-order compact schemes. *Journal of Computational Physics*, 111:220–236, 1994.

[8] A. Chaudhuri, A. Hadjadj, and A. Chinnayya. On the use of immersed boundary methods for shock/obstacle interactions. *Journal of Computational Physics*, 230(5), 2011.

[9] A. W Cook and W. H Cabot. A high-wavenumber viscosity for high-resolution numerical methods. *Journal of Computational Physics*, 195(2):594–601, 2004.

[10] P. A. Cundall and O. Strack. A discrete numerical model for granular assemblies. *Geotechnique*, 29(1):47–65, 1979.

[11] F. Ducros, V. Ferrand, F. Nicoud, C. Weber, D. Darracq, C. Gacherieu, and T. Poinsot. Large-eddy simulation of the shock/turbulence interaction. *Journal of Computational Physics*, 152(2):517–549, 1999.

[12] R. O. Fox. A kinetic-based hyperbolic two-fluid model for binary hard-sphere mixtures. *Journal of Fluid Mechanics*, 877:282–329, 2019.

[13] E. Franquet, V. Perrier, S. Gibout, and P. Bruel. Free underexpanded jets in a quiescent medium: A review. *Progress in Aerospace Sciences*, 77:25–53, 8 2015.

[14] J. B. Freund. Proposed inflow/outflow boundary condition for direct computation of aerodynamic sound. *AIAA Journal*, 35(4):740, 1997.

[15] D. Gidaspow. *Multiphase flow and fluidization: continuum and kinetic theory descriptions.* Academic press, 1994.

[16] DJ Gunn. Transfer of heat or mass to particles in fixed and fluidised beds. *International Journal of Heat and Mass Transfer*, 21(4):467–476, 1978.

[17] C. B. Henderson. Drag coefficients of spheres in continuum and rarefied flows. *AIAA Journal*, 14(6):707–708, 1976.

[18] T. R. Hendrickson, A. Kartha, and G. V. Candler. An improved Ducros sensor for the simulation of compressible flows with shocks. In *2018 Fluid Dynamics Conference*, page 3710, 2018.

[19] Z. Hosseinzadeh-Nik, S. Subramaniam, and J. D. Regele. Investigation and quantification of flow unsteadiness in shock-particle cloud interaction. *International Journal of Multiphase Flow*, 101:186–201, 2018.

[20] R. W. Houim and E. S. Oran. Numerical simulation of dilute and dense layered coal-dust explosions. *Proceedings of the Combustion Institute*, 35(2):2083 – 2090, 2015. ISSN 1540-7489.

[21] S. Kawai, S. K. Shankar, and S. K. Lele. Assessment of localized artificial diffusivity scheme for large-eddy simulation of compressible turbulent flows. *Journal of Computational Physics*, 229(5):1739–1762, 2010.

[22] A.K. Kulkarni, M. Kumar, and K.K. Kuo. Review of solid-propellant ignition studies. *AIAA Journal*, 20(2):243–244, 1982.

[23] S. K. Lele. Compact finite difference schemes with spectral-like resolution. *Journal of Computational Physics*, 103(1):16–42, 1992.

[24] Y. Ling, A. Haselbacher, and S. Balachandar. Importance of unsteady contributions to force and heating for particles in compressible flows: Part 1: Modeling and analysis for shock–particle interaction. *International Journal of Multiphase Flow*, 37(9):1026–1044, 2011.

[25] Y. Ling, J. L. Wagner, S. J. Beresh, S. P. Kearney, and S. Balachandar. Interaction of a planar shock wave with a dense particle curtain: Modeling and experiments. *Physics of Fluids*, 24(11):113301, 2012.

[26] E. Loth. Compressibility and rarefaction effects on drag of a spherical particle. *AIAA Journal*, 46(9):2219–2228, 2008.

[27] K. Mattsson, M. Svärd, and J. Nordström. Stable and accurate artificial dissipation. *Journal of Scientific Computing*, 21(1):57–79, 2004.

[28] J. B. McLaughlin. Inertial migration of a small sphere in linear shear flows. *Journal of Fluid Mechanics*, 224:261–274, 1991.

[29] M. Mehrabadi, S. Tenneti, R. Garg, and S. Subramaniam. Pseudo-turbulent gas-phase velocity fluctuations in homogeneous gas–solid flow: fixed particle assemblies and freely evolving suspensions. *Journal of Fluid Mechanics*, 770:210–246, 2015.

[30] M. Mehta, A. Sengupta, N. O. Renno, J. W. Van Norman, P. G. Huseman, D. S. Gulick, and M. Pokora. Thruster plume surface interactions: Applications for spacecraft landings on planetary bodies. *AIAA Journal*, 51(12):2800–2818, 2013.

[31] Y. Mehta, C. Neal, K. Salari, T. L. Jackson, S. Balachandar, and S. Thakur. Propagation of a strong shock over a random bed of spherical particles. *Journal of Fluid Mechanics*, 839:157–197, 2018.

[32] Y. Mehta, T. L. Jackson, and S. Balachandar. Pseudo-turbulence in inviscid simulations of shock interacting with a bed of randomly distributed particles. *Shock Waves*, pages 1–14, 2019.

[33] J. Mohd-Yusof. Combined immersed-boundary/B-spline methods for simulations of flow in complex geometries. *Center for turbulence research annual research briefs*, 161(1):317–327, 1997.

[34] J. Nordström and M. Svärd. Well-posed boundary conditions for the Navier–Stokes equations. *SIAM Journal on Numerical Analysis*, 43(3):1231–1255, 2005.

[35] A. N. Osnes, M. Vartdal, M. G. Omang, and B. A. P. Reif. Computational analysis of shock-induced flow through stationary particle clouds. *International Journal of Multiphase Flow*, 114:268–286, 2019.

[36] A. N. Osnes, M. Vartdal, M. G. Omang, and B. A. P. Reif. Particle-resolved simulations of shock-induced flow through particle clouds at different Reynolds numbers. *arXiv preprint arXiv:1906.08299*, 2019.

[37] M. Parmar, A. Haselbacher, and S. Balachandar. Modeling of the unsteady force for shock–particle interaction. *Shock Waves*, 19(4):317–329, 2009.

[38] M. Parmar, A. Haselbacher, and S. Balachandar. Improved drag correlation for spheres and application to shock-tube experiments. *AIAA Journal*, 48(6):1273–1276, 2010.

[39] M. Parmar, A. Haselbacher, and S. Balachandar. Generalized Basset-Boussinesq-Oseen equation for unsteady forces on a sphere in a compressible flow. *Physical Review Letters*, 106(8):084501, 2011.

[40] M. Parmar, A. Haselbacher, and S. Balachandar. Equation of motion for a sphere in non-uniform compressible flows. *Journal of Fluid Mechanics*, 699:352–375, 2012.

[41] M. Patel, J. Rabinovitch, and J. Capecelatro. Eulerian–lagrangian simulations of plume-induced sheared granular beds under martian conditions. In *AIAA SCITECH 2022 Forum*, page 2193, 2022.

[42] S. Pirozzoli. Stabilized non-dissipative approximations of Euler equations in generalized curvilinear coordinates. *Journal of Computational Physics*, 230(8):2997–3014, 2011.

[43] G.D. Roy, S.M. Frolov, A.A. Borisov, and D.W. Netzer. Pulse detonation propulsion: challenges, current status, and future perspective. *Progress in Energy and Combustion Science*, 30(6):545 – 672, 2004. ISSN 0360-1285.

[44] G. S. Shallcross, R. O. Fox, and J. Capecelatro. A volume-filtered description of compressible particle-laden flows. *International Journal of Multiphase Flow*, 122:103138, 2020.

[45] B. Strand. Summation by parts for finite difference approximations for d/dx. *Journal of Computational Physics*, 110(1):47–67, 1994.

[46] M. Svärd and J. Nordström. A stable high-order finite difference scheme for the compressible navier–stokes equations: no-slip wall boundary conditions. *Journal of Computational Physics*, 227(10), 2008.

[47] M. Svärd, M. H. Carpenter, and J. Nordström. A stable high-order finite difference scheme for the compressible Navier–Stokes equations, far-field boundary conditions. *Journal of Computational Physics*, 225(1):1020–1038, 2007.

[48] S. Tenneti, R. Garg, and S. Subramaniam. Drag law for monodisperse gas–solid systems using particle-resolved direct numerical simulation of flow past fixed assemblies of spheres. *International Journal of Multiphase Flow*, 37(9):1072–1092, 2011.

[49] T. G. Theofanous, V. Mitkin, and C.-H. Chang. Shock dispersal of dilute particle clouds. *Journal of Fluid Mechanics*, 841:732–745, 2018.

[50] R. Vishnampet Ganapathi Subramanian. *An exact and consistent adjoint method for high-fidelity discretization of the compressible flow equations.* PhD thesis, University of Illinois at Urbana-Champaign, 2015.

[51] A. M. Worthington. Xxviii. on the forms assumed by drops of liquids falling vertically on a horizontal plate. *Proceedings of the Royal Society of London*, 25(171-178):261–272, 1877.

[52] Y. Yao, G. S. Shallcross, R. Ni, T. Kim, M. Mehta, J. Rabinovitch, and J. Capecelatro. The dynamics of inertial particles in under-expanded jets: A numerical study. In *AIAA Scitech 2020 Forum*, page 1327, 2020.